JURNAL KIMIA VALENSI
p-ISSN: 2460-6065; e-ISSN: 2548-3013
Journal homepage: https://journal.uinjkt.ac.id/index.php/valensi
Research Article

Preparation of Thin Film $CuSnO_3$ by Dip Coating Method: Structural, Optical, and Electrical Properties for Dye-Sensitized Solar Cell Applications

Hary Sanjaya[1,2*], Hermansyah Aziz[2], Yeni Stiadi[2], Syukri Arief[2], Yohandri[3], Septian Budiman[4,5]

[1]*Department of Chemistry, Universitas Negeri Padang, Jln. Hamka, Padang, 25132, Indonesia*
[2]*Departement of Chemistry, Andalas University, Jln, Limau Manis Kec. Pauh, Padang, 25175, Indonesia*
[3]*Department of Physic, Universitas Negeri Padang, Jln. Hamka, Padang, 25132, Indonesia*
[4]*Metallurgy and Materials Science Research Institute, Chulalongkorn University, Bangkok, 10330, Thailand*
[5]*Interdisciplinary Program of Nanoscience and Technology, College of Interdisciplinary and Integrative Studies, Chulalongkorn University, Pathumwan, Bangkok, 10330, Thailand*

Email: hary.s@fmipa.unp.ac.id

Article Info
Received: Marc 03,2026
Revised: May 12, 2026
Accepted: May 14, 2026
Online: June 6, 2026

Citation:
Sanjaya, H., Aziz, H., Stiadi, Y., Arief, A., Yohandri., Budiman, S. (2026). Preparation of Thin Film $CuSnO_3$ by Dip Coating Method : Structural, Optical, and Electrical Properties for Dye-Sensitized Solar Cell Applications. *Jurnal Kimia Valensi*, 12(1), 110-118.

Doi: 10.15408/jkv.v12i1.50326

Abstract

This study addresses the critical need for cost-effective, earth-abundant alternatives to Indium Tin Oxide (ITO) by developing transparent and conductive Copper Stannate ($CuSnO_3$) thin films via sol-gel dip-coating. Using diethanolamine (DEA) and monoethanolamine (MEA) as chelating agents to enhance film stability and uniformity, the synthesized films were calcined at 550 °C, yielding predominantly amorphous structures that minimize grain boundary recombination. Characterization revealed crack-free morphologies with a thickness of approximately 1.88 µm, while optical analysis showed band gap energies ranging from 2.16 eV (DEA) to 2.31 eV (MEA), suitable for visible-light absorption. Electrical measurements indicated significant improvements in conductivity, with MEA-modified films achieving 173.58 S/m and DEA-modified films reaching 3600 S/m.When used as photoelectrodes in Dye-Sensitized Solar Cells (DSSCs) with natural sensitizers, the films demonstrated successful photovoltaic performance, with Quercetin yielding the highest power conversion efficiency of 0.26%, thereby validating solution-processed amorphous $CuSnO_3$ as a viable, low-cost material for scalable optoelectronic applications.

Keywords: Amorphous oxide semiconductor, copper Stannate ($CuSnO_3$), dye-sensitized solar cells (DSSC), sol-gel dip-coating, thin films

1. INTRODUCTION

The rapid advancement of renewable energy technologies has intensified the demand for cost-effective, transparent, and electrically conductive oxide semiconductors. Indium tin oxide (ITO), despite its widespread use, faces critical limitations including high material cost, scarcity of indium, mechanical brittleness, and diffusion-induced performance degradation in optoelectronic devices [1]. Consequently, alternative oxide semiconductors composed of earth-abundant elements have attracted increasing research interest [2,3].

Copper stannate ($CuSnO_3$) is an emerging amorphous oxide semiconductor characterized by a moderate optical band gap (2.0–2.5 eV), good electrical conductivity, and compatibility with solution-based processing [4]. Previous studies have demonstrated its applicability in transparent conducting oxides, photoelectrochemical systems, and lithium-ion battery anodes [5]. Notably, the amorphous phase of $CuSnO_3$ has been reported to enhance charge transport stability and optical absorption in the visible region, making it attractive for photovoltaic applications such as dye-sensitized solar cells (DSSCs) [6,7].

Among various fabrication techniques, the sol–gel dip-coating method offers significant advantages, including low processing temperature, large-area coating capability, compositional homogeneity, and cost efficiency [8]. The incorporation of chelating agents such as diethanolamine (DEA) plays a crucial role in stabilizing metal precursors, controlling hydrolysis–

condensation kinetics, and improving film uniformity. Moreover, the Monoethanolamine (MEA), with its smaller molecular size and higher basicity, has been employed in sol-gel processing of ZnO and SnO_2 to tailor particle size and solution stability; however, its effect on $CuSnO_3$ thin-film properties has not been explored. However, excessive additive concentration may induce phase segregation or secondary oxide formation [9,10]. MEA, being a primary amine with only one hydroxyl group, offers a different chelation mechanism compared to DEA, likely producing smaller precursor aggregates and different decomposition behaviour. A systematic comparison of these two alkanolamines is therefore expected to reveal how the chelating agent structure influences the structural, optical, and electrical properties of $CuSnO_3$ thin films.

This study aims to systematically investigate the influence of MEA and DEA concentration on the physicochemical properties of $CuSnO_3$ thin films prepared via dip-coating. Particular emphasis is placed on band gap modulation, structural evolution, surface morphology, and electrical conductivity, with a view toward optimizing film performance for DSSC applications.

2. RESEARCH METHODS

Materials

Copper(II) nitrate trihydrate ($Cu(NO_3)_2 \cdot 3H_2O$), tin(II) chloride dihydrate ($SnCl_2 \cdot 2H_2O$), diethanolamine (DEA), monethanolamine (MEA), ethanol, and deionized water were used as received without further purification. Microscope glass slides served as substrates.

Preparation of $CuSnO_3$ Sol

A precursor sol was prepared by dissolving stoichiometric amounts of $Cu(NO_3)_2 \cdot 3H_2O$ and $SnCl_2 \cdot 2H_2O$ in ethanol under continuous magnetic stirring. MEA and DEA were added in 2 ml volumes dropwise to act as a complexing and stabilizing agent. The solution was stirred until a clear and homogeneous sol was obtained and subsequently aged at room temperature to enhance sol stability [4].

Thin Film Deposition via Dip-Coating

Glass substrates were ultrasonically cleaned in ethanol and deionized water prior to coating. Dip-coating was performed by immersing the substrates in the sol for 20 minutes, followed by vertical withdrawal at a constant speed. The coated films were dried and then calcined at 550 °C to remove organic residues and promote the formation of the oxide network.

The counter electrode preparation

The counter electrode was prepared on ITO glass coated with carbon obtained from the smoke of a burning candle. The carbon coating on the ITO glass involved coating the conductive side of the ITO glass with wax to form a black layer. The ITO glass was smoothed out using a cotton swab, and the carbon layer was shaped to a size of 1 cm x 1 cm.

DSSC Assembly

The CSO ($CuSnO_3$) glass was formed into a size of 1 x 1 cm using Scotch tape. The dip-coating method was used to deposit $CuSnO_3$ paste on the glass preparation area, then the $CuSnO_3$ layer was immersed in a solution of purple sweet potato dye, quercetin, and tannic acid with a soaking time of 30 minutes, after which it was allowed to dry. The $CuSnO_3$ layer was covered with a carbon counter electrode to form a sandwich structure with the ends offset by 0.25 cm for electrical contact, then clamped on both sides with binder clips. Drop 2 drops of electrolyte between the two electrode spaces. The DSSC is ready to be tested for voltage and resistance [11].

Characterization

Optical properties were evaluated using UV–Vis diffuse reflectance spectroscopy (DRS), and band gap energies were calculated using the Kubelka–Munk method. *Fourier Transform Infrared* (FTIR) is an effective method for struktural analgesia, which can be compared with other optical devices. Structural analysis was conducted by X-ray diffraction (XRD). Surface morphology was examined using scanning electron microscopy (SEM). Electrical conductivity was measured using the four-point probe (FPP) technique. The efficiency of a DSSC can be determined by measuring the resistance and voltage using a digital multimeter and a potentiostat. From these measurements, the resulting current can be calculated using a equation (1).

$$V = I \times R \quad (1)$$

Where:
V: Voltage (Volts)
I: Current (Amperes)
R: Resistance (Ω, Ohms)

The efficiency of DSSC can be calculated using the equation (2).

$$\eta = \frac{Pmax}{Pin} X\ 100\% \quad (2)$$

Maximum power provided by the link:

$$P_{max} = V_{max} \times I_{max} \quad (3)$$

Where:
η : DSSC efficiency (%)
P_{max} : incident power from the light source used (input) on the DSSC cell (Watts)
V_{max} : maximum voltage (Volts).

3. RESULTS AND DISCUSSION

Optical Properties

UV-Vis DRS spectra showed strong visible-region absorption for all samples. The calculated band gaps are listed in **Table 1**. The film prepared with 2.0 mL DEA exhibited the lowest band gap (2.16 eV), while the MEA-modified film showed a band gap of 2.31 eV. The smaller band gap in the DEA-modified sample is The band gap of 2.16 eV obtained with DEA addition is slightly narrower than the 2.2 eV reported by Kim et al. for amorphous $CuSnO_3$, likely due to the different chelating environment [4]. Zhu et al. observed a similar band gap narrowing in $CuSnO_3/In_2O_3$ composites, supporting the trend that organic modifiers can influence the electronic structure of the oxide matrix[10].

Table 1. Optical band gap values of modified $CuSnO_3$ thin films

Additive	Band Gap value
MEA	2.31 eV
DEA	2.16 eV

Semiconductor materials have an energy gap between 0-4 eV, meaning they can conduct electricity well if they have a narrow band gap. The smaller a material's energy gap, the greater its potential for application in various fields. This is because electrons are more easily excited when the energy gap is small, so the material can better generate electricity due to the resulting electron transfer [11].

The decrease in the energy gap value along with the modification of the additives used can be caused by the quality of the resulting layer. The longer the carbon chain of the modifier used, the more transparent the layer formed because more molecules are involved and influence the agglomeration process. The energy gap shows the movement of electrons from the valence band to the conduction band, the energy absorbed by the material increases with increasing absorption value, causing the energy gap value to decrease [12,13].

Structural Analysis

XRD patterns revealed that $CuSnO_3$ films predominantly exhibited an amorphous structure, consistent with previous reports. At higher DEA concentrations, a weak diffraction peak corresponding to tetragonal SnO_2 was observed, suggesting partial phase segregation (**Figure 1**). The amorphous phase is advantageous for DSSC applications due to reduced grain boundary recombination.

The XRD pattern of pure $CuSnO_3$ (without additives) shows broad amorphous features, along with weak crystalline peaks at $2\theta \approx 20.5°$ and 42.8°, corresponding to tetragonal SnO_2 and monoclinic CuO, respectively. This indicates partial phase segregation, as also reported by Kim et al.[4]. In contrast, the film prepared with 2 mL DEA exhibits only a single weak SnO_2 peak at ~20.6°, while the CuO peak is absent. This suggests that DEA preferentially stabilises copper ions in the amorphous network, suppressing CuO crystallisation. The MEA-modified films (**Figure 2**) display solely an amorphous halo, indicating that MEA is even more effective in preventing phase separation [6].

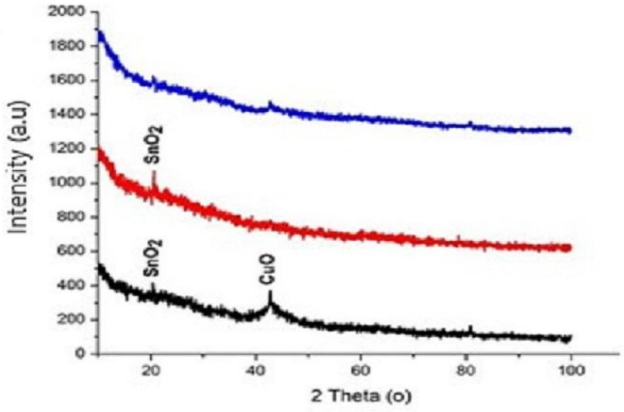

Figure 1. XRD patterns of $CuSnO_3$ thin films prepared under different conditions: without additives (black), with 2 ml of DEA (red), and with a 20-minute dipping time (blue). Peaks corresponding to SnO_2 and CuO phases are identified

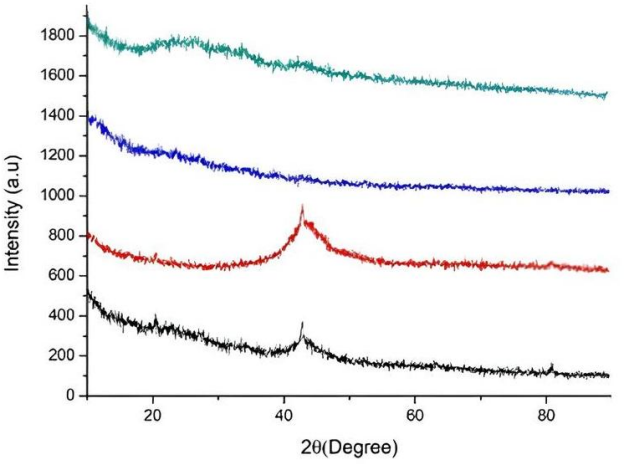

Figure 2. XRD patterns of thin films prepared with varying molar concentrations of MEA additive: 0 M (Black), 0.025 M (Red), 0.05 M (Blue), and 0.075 M (Green)

The XRD patterns of the $CuSnO_3$ thin films prepared with varying MEA concentrations (Figure 2) are compiled in the table. All samples, regardless of MEA content, exhibit a single, broad diffuse scattering band that extends from approximately 15° to 40° (2θ) and decays gradually toward higher angles. No sharp diffraction peaks are detected in any of the patterns. This hallmarks a predominantly amorphous structure with only short-range atomic order. The amorphous

halo is centered around 20–30°, which is characteristic of the short-range metal–oxygen correlations in amorphous copper-stannate networks and agrees with earlier reports on sol–gel-derived $CuSnO_3$[4,14].

Crucially, the amorphous signature is preserved even in the 0 M MEA (control) sample, prepared from the same precursor solution but without a chelating agent. In earlier experiments (**Figure 1**), the same precursor formulation without any organic modifier yielded distinct crystalline peaks of tetragonal SnO_2 (20.6°) and monoclinic CuO (42.8°). The absence of these phases in the present series indicates that the specific synthesis conditions used here—possibly slightly different precursor concentrations or hydrolysis rates—produce an amorphous oxide even in the absence of MEA. However, this does not diminish the unique impact of MEA. Specifically, the addition of MEA reinforces the amorphous nature and uniquely prevents the nucleation of crystalline secondary phases as calcination proceeds, underscoring its essential role in the process.

As the MEA concentration is increased from 0.025 M to 0.075 M, the overall intensity of the amorphous halo decreases slightly (e.g., the intensity at 20° drops from 1750 a.u. for 0.025 M to 1600 a.u. for 0.075 M). This gradual reduction can be attributed to a subtle change in film thickness or mass density; higher MEA loadings may produce thinner, more compact films after calcination because the amine lowers the surface tension and enhances wetting during dip-coating, leading to a smaller deposited amount per withdrawal cycle. The consistent amorphous profile, however, demonstrates that MEA suppresses crystallization effectively even at the lowest concentration tested (0.025 M).

The structural findings have direct implications for the performance of dye-sensitized solar cells. An amorphous oxide photoanode lacks grain boundaries, which are notorious for trapping electrons and promoting recombination with the electrolyte. The fully amorphous nature of the MEA-modified films, therefore, supports enhanced charge-transport stability. Furthermore, the absence of phase segregation (SnO_2 or CuO) guarantees a homogeneous electronic landscape, which is beneficial for uniform dye adsorption and consistent photocurrent generation. When combined with the favorable band gaps (2.16–2.31 eV) and the conductivities measured earlier, these amorphous $CuSnO_3$ layers emerge as a viable low-cost alternative to crystalline TiO_2 photoanodes, especially where solution-based, large-area processing is required.

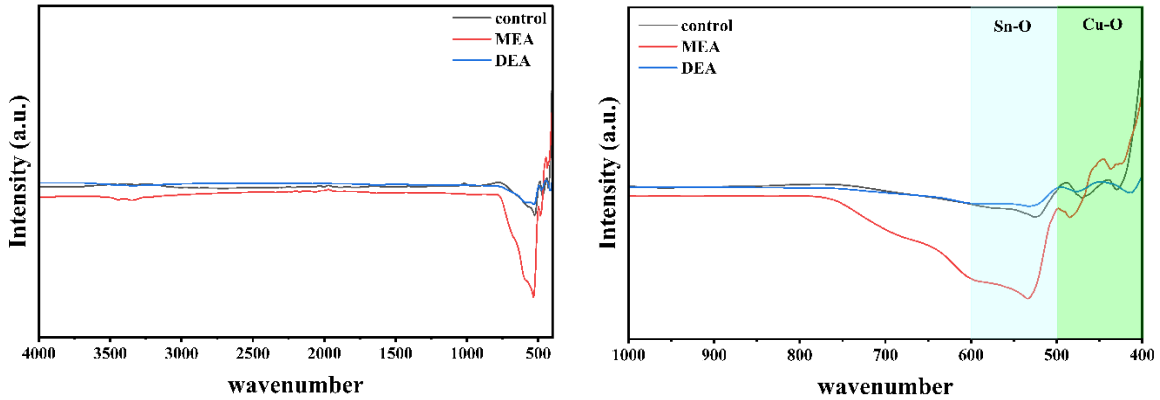

Figure 3. FTIR spectra of $CuSnO_3$ thin films synthesized with different organic modifiers (MEA and DEA) compared to a control sample.

Figure 3 shows the chemical composition and functional groups of the synthesized $CuSnO_3$ thin films, which were evaluated by Fourier Transform Infrared (FTIR) spectroscopy in the 1000-400 cm^{-1} range, a region typically associated with lattice vibrations in metal oxides. All samples exhibited characteristic absorption bands below 600 cm^{-1}, confirming the successful formation of the $CuSnO_3$ inorganic framework. Specifically, the peaks observed in the 400–500 cm^{-1} and 550–600 cm^{-1} ranges correspond to the stretching modes of Cu–O and Sn–O bonds, respectively. The intensity of these vibrations was significantly influenced by the choice of organic modifier; the MEA-modified sample displayed the most prominent absorption peaks at approximately 535 cm^{-1} and 450 cm^{-1}, suggesting that Monoethanolamine (MEA) facilitates a denser network of metal-oxygen bonds compared to the DEA-modified and control samples. While the DEA-modified film showed a flatter spectral response, its superior electrical conductivity—observed in previous measurements—suggests that electronic performance in these films may be more closely tied to the narrower band gap (2.16 eV) than to the sheer density of infrared-active surface vibrations. Overall, the FTIR data verify that the precursors successfully transitioned into a stable metal-oxide matrix suitable for photovoltaic applications [15,16].

Although MEA promotes a denser metal-oxygen bonding framework (as indicated by

stronger IR absorption), the DEA-modified film showed a narrower optical band gap (2.16 eV vs. 2.31 eV for MEA) and higher conductivity. This suggests that electronic conduction in these amorphous films is primarily governed by the energetic position and width of the band tails, which are more favorably modified by DEA, rather than by the mere density of M–O bonds. DEA's larger molecular structure may introduce a higher degree of disorder that creates more shallow donor states, enhancing conductivity.

Morphology and Thickness

SEM images showed uniform, crack-free films with increasing surface compactness as dipping time increased. The morphological results of the synthesis of $CuSnO_3$ thin films by dip-coating at 550 °C showed fine grains with almost uniform sizes, with diameters of 0.97-1.14 μm at a magnification of 2500×. At a magnification of 25000 times, the thickness of the $CuSnO_3$ thin film was 1.883 μm. This thickness will later be used to calculate the resistivity.

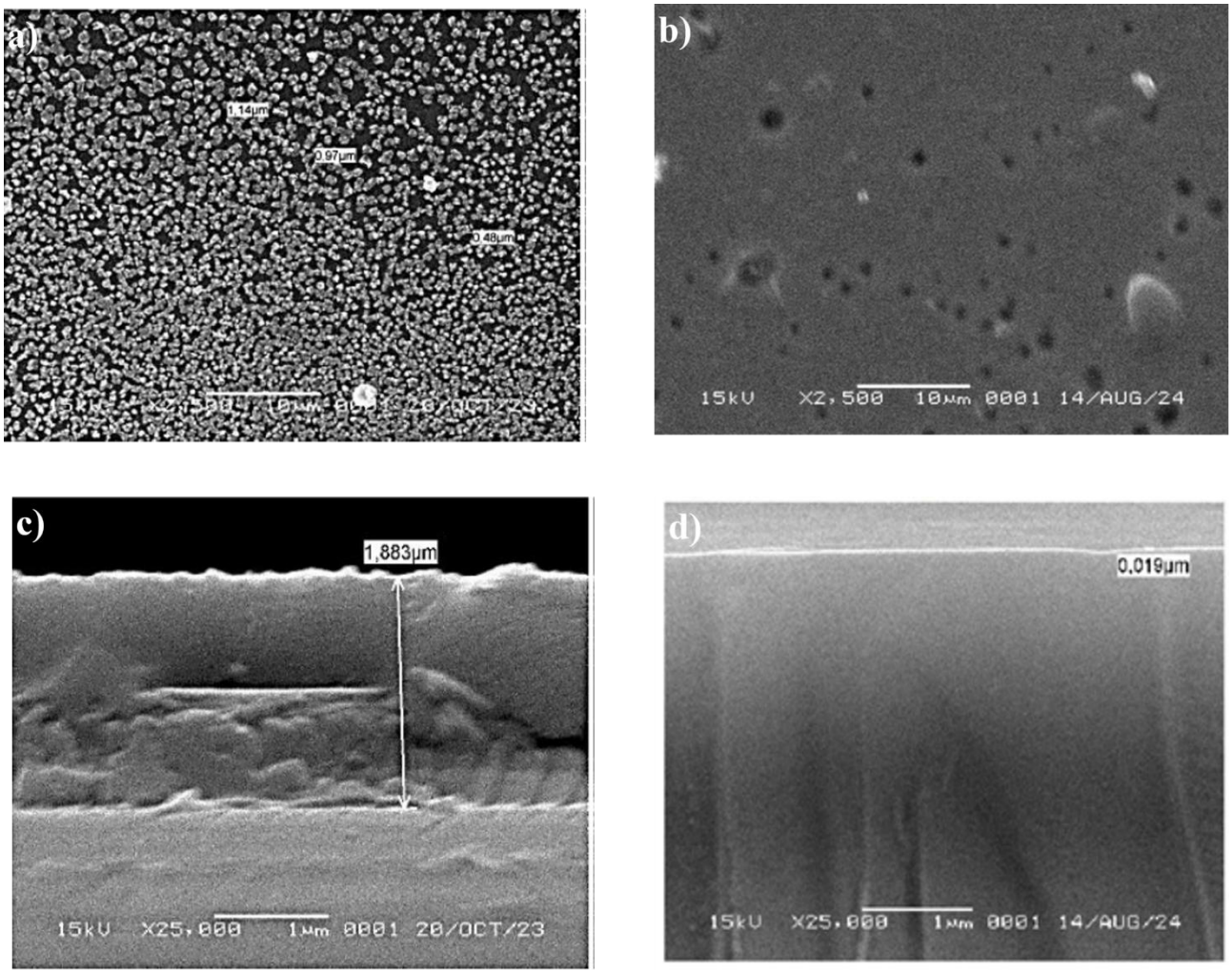

Figure 4. SEM analysis of $CuSnO_3$ thin films: (a) Top-view morphology showing granular surface distribution of MEA, (b) Top-view morphology showing granular surface distribution of DEA, (c) Cross-sectional view showing a total thickness of MEA, and (d) Cross-sectional view showing a total thickness of DEA.

The characterization results in **Figure 4**(a)–(d) present the surface and cross-sectional SEM images of $CuSnO_3$ thin films prepared with MEA and DEA. The top-view micrographs (a and b) reveal that both films are continuous, crack-free, and composed of densely packed granular structures, indicating successful sol-gel dip-coating and calcination. The MEA-modified film (a) displays fine, equiaxed grains with a narrow size distribution in the range 0.97–1.14 μm, resulting in a homogeneous surface with minimal void spaces. In contrast, the DEA-modified film (b) exhibits slightly coarser and more irregular grains, along with a marginally higher surface roughness. This difference is attributed to the larger molecular size and stronger chelating ability of DEA, which influences the aggregation of precursor clusters during sol aging and the subsequent densification during thermal treatment. Cross-sectional analysis (c and d) shows that both films are well-adhered to the glass substrate and possess a uniform thickness across the imaged area. The MEA-modified film (c) has a measured thickness of approximately 1.88 μm, while

the DEA-modified film (d) yields a comparable thickness, indicating that both additives produce films within the same thickness window under identical dip-coating conditions. The similarity in thickness suggests that the observed differences in electrical conductivity (3600 S/m for DEA vs. 173.58 S/m for MEA) and optical band gap (2.16 eV vs. 2.31 eV) are primarily governed by the local atomic structure and the degree of electronic disorder rather than by simple geometrical factors. The fully amorphous nature of the MEA film (confirmed by XRD) yields a smooth and uniform morphology that favors low scattering losses, while the DEA film's slightly rougher surface and embedded SnO_2 nanocrystallites create additional electronic pathways that enhance conductivity despite a marginal loss in transparency. Overall, the SEM analysis confirms that the choice of chelating agent enables fine-tuning of the film's microstructural features, allowing a deliberate trade-off between morphological uniformity and electrical performance for dye-sensitized solar cell applications. Further optimization of the additive concentration and withdrawal speed is expected to precisely control the thickness and grain characteristics, thus maximizing the photovoltaic efficiency of $CuSnO_3$-based DSSCs [6].

With these results, it can be seen that the thin layer of $CuSnO_3$ is still thick based on the theory that a thin layer is >1 μm [17]. The thicker the resulting layer, the less transparent its properties. An increase in film thickness was directly associated with a reduction in optical transparency. As the deposited layer thickens, light transmission through the film decreases due to increased absorption and scattering within the material. This effect arises from the longer optical path length and the increased density of the deposited particles, which promote photon–matter interactions. Additionally, thicker films tend to exhibit higher surface roughness and a greater likelihood of structural defects, both of which contribute to increased optical losses. Consequently, while thicker layers may improve coverage uniformity and electrical or mechanical properties, they compromise transparency, highlighting the need for careful optimization of film thickness depending on the targeted application [18,19].

Electrical Conductivity

Electrical measurements demonstrated a significant increase in conductivity with both DEA and MEA. To determine the conductivity of the thin $CuSnO_3$ layer, electrical resistance was measured using a 4-point probe system. The $CuSnO_3$ thin layer, with a 20-minute dip, yielded a voltage of 14.8 V and a current of 0.63 A, resulting in a resistance of 277.76 × 10^{-6} Ωm(**Table 2**). The resistance value affects the number of ions deposited on the substrate. If the resistance value is small, the current flowing is large due to the large number of ions deposited, and vice versa.

Table 2. Electrical properties of modified $CuSnO_3$ thin films

Modifier	Electrical conductivity (S/m)	Electrical resistivity (Ωm)
MEA	173.58	5761 x 10^{-6}
DEA	3600	277.76 x 10^{-6}

The resistance value is directly proportional to the voltage, so a higher resistance means a higher voltage, and it is inversely proportional to the current, so a higher resistance means a lower current. A higher resistance value also increases resistivity, as resistance and resistivity are directly proportional [20].

The distinct particle morphologies observed by SEM for the MEA- and DEA-modified films correlate directly with their electrical conductivity values. The MEA film (**Figure 4a**) exhibits fine, equiaxed grains with an average diameter of ~1 μm and a highly compact, uniform surface. This fine-grained structure introduces a high density of grain boundaries (or inter-granular regions) that act as scattering centres for charge carriers, thereby increasing the film resistivity. Consequently, the MEA-modified film yields a moderate conductivity of 173.58 S m^{-1}. In contrast, the DEA-modified film (Figure 4b) shows noticeably coarser and more irregular grains, accompanied by a rougher surface. The larger grains reduce the overall density of grain boundaries, decreasing carrier scattering and facilitating more efficient inter-particle charge transport. Moreover, XRD analysis (**Figure 1**) revealed that the DEA film contains embedded tetragonal SnO_2 nanocrystallites, which can serve as highly conductive pathways within the amorphous $CuSnO_3$ matrix, analogous to the beneficial role of secondary conductive phases in transparent oxide conductors. These combined effects—larger grains, fewer grain boundaries, and crystalline SnO_2 inclusions—explain the significantly higher conductivity of 3600 S m^{-1} (36.0 S cm^{-1}) measured for DEA. This grain-size-dependent conductivity trend is consistent with classic grain-boundary trapping models, where smaller crystallites lead to higher potential barriers and reduced carrier mobility (Seto, 1975; Minami, 2000). Thus, the SEM-derived particle size not only confirms the structural differences induced by the chelating agent but also provides a consistent microstructural basis for the observed order-of-magnitude difference in electrical performance. Future optimisation may target an intermediate grain size that balances high conductivity with the crack-free, homogeneous surfaces required for stable DSSC photoanodes [21].

In this study, a resistivity value of 277.76 × 10^{-6} Ωm was obtained for the DEA-modified film, corresponding to a conductivity of 3600 S/m. Pornsiri et al. found that electrical conductivity increases with increasing grain size of the surface of the resulting thin film [22]. On the other hand, in the sample of MEA-modified film, a resistivity value of 5761 x 10^{-6} Ωm was obtained with a conductivity value of 173.58 S/m. The relationship between conductivity and resistivity is inversely proportional; the greater the resistivity, the smaller the electrical conductivity, because resistivity, as a clear inhibitor, is the opposite of conductivity as a conductor of electric current [23].

Potential Application in DSSCs

The optimized $CuSnO_3$ thin films exhibit suitable band gap energy, high optical absorption, and enhanced electrical conductivity, making them promising candidates as photoelectrode or interfacial layers in dye-sensitized solar cells. Their low-cost fabrication and compatibility with large-area processing further support their practical application.

Table 3. Photovoltaic performance DEA-modified film of DSSCs sensitized with various natural dyes

Dye Source	V_{max} (V)	I_{max} (mA)	P_{max} (mW)	Efficiency (%)
Quercetin	0.33	1.29×10^{-3}	0.4257×10^{-3}	0.26
Tannic Acid	0.289	1.13×10^{-3}	0.326×10^{-3}	0.20
Purple Sweet Potato	0.265	1.04×10^{-3}	0.276×10^{-3}	0.17

The study evaluated the photovoltaic performance of Dye-Sensitized Solar Cells (DSSC) using three distinct natural sensitizers: purple sweet potato , quercetin , and tannic acid. All measurements were conducted under a light intensity of 196 Lux, corresponding to a calculated power input (P_{in}) of 0.1619 mW/cm^2. Among the tested dyes, Quercetin exhibited the highest performance, achieving an efficiency (η) of 0.26% (**Table 3**). This was driven by a maximum voltage (Vmax) of 0.330 V and a current (Imax) of 1.29\times 10^{-3}mA, resulting in a peak power output (Pmax) of 0.4257 times 10^{-3} mW. Tannic Acid followed with a moderate efficiency of 0.20%. It generated a voltage of 0.289 V and a current of 1.13 × 10^{-3} mA, yielding a power output of 0.326 × 10^{-3} mW. Finally, the Purple Sweet Potato dye demonstrated the lowest efficiency at 0.17%. This sample produced the lowest electrical parameters, with a voltage of 0.265 V and a current of 1.04 \times 10-3 mA, leading to a power output of 0.276\times 10^{-3} mW. These results indicate that, under the specific conditions of this experiment, quercetin exhibits superior charge-transfer or light-absorption properties compared to the other two natural dyes.

The fabricated DSSCs exhibited power conversion efficiencies of 0.26%, 0.20%, and 0.17%, confirming the devices' successful photovoltaic operation. Although these efficiency values are lower than those reported for fully optimized DSSCs employing conventional TiO_2 photoanodes and liquid or ionic liquid electrolytes, they are consistent with DSSC systems based on non-optimized thin films and newly developed material architectures. The observed decrease in efficiency can be attributed to limitations in charge transport and interfacial charge-transfer kinetics, which are strongly influenced by thin-film properties such as thickness, transparency, and morphology. As discussed in previous studies, excessive film thickness or increased structural density can reduce light transmittance and hinder electron transport, while higher internal resistance and recombination at the semiconductor–electrolyte interface further suppress photocurrent generation. Importantly, the systematic trend in efficiency demonstrates a clear structure–performance relationship, indicating that variations in thin-film characteristics directly affect DSSC performance. These results highlight the functional viability of the thin films in DSSC applications and suggest that further optimization of film thickness, porosity, and interfacial engineering could significantly enhance device efficiency.

The efficiency of dye-sensitized solar cells (DSSCs) is strongly governed by the properties of the thin films employed in the photoanode and electrolyte system, as these layers directly influence light harvesting, charge transport, and interfacial recombination processes. Optimized thin films facilitate effective dye loading and ensure sufficient optical transparency while maintaining continuous electron pathways within the mesoporous structure. However, deviations from optimal film characteristics—such as excessive thickness, increased viscosity in gel electrolytes, or nanoparticle agglomeration—can impede ionic diffusion and elevate charge-transfer resistance [24], ultimately reducing power conversion efficiency. As demonstrated in the reported DSSC systems, polymer gel electrolytes and nanocomposite films exhibited efficiencies comparable to liquid electrolytes when their structural and transport properties were carefully controlled, whereas higher nanoparticle loadings led to increased internal resistance and diminished current density [25]. These findings highlight that DSSC efficiency is not solely determined by material composition, but by a delicate balance between thin-film morphology, thickness, ionic mobility, and interfacial charge transfer, underscoring the critical

role of thin-film optimization in achieving high-performance DSSCs [26].

4. CONCLUSIONS

This study set out to develop a low-cost, earth-abundant alternative to ITO by preparing transparent and conductive Copper Stannate ($CuSnO_3$) thin films using a simple sol-gel dip-coating method. The research successfully compared how two different chelating agents, diethanolamine (DEA) and monoethanolamine (MEA), influence the final film properties. The key findings show that both agents produced smooth, crack-free, and predominantly amorphous films about 1.88 µm thick. This amorphous structure is beneficial as it minimizes energy-wasting electron recombination. A clear difference was observed: the MEA-modified film had a wider band gap (2.31 eV) and moderate conductivity, while the DEA-modified film achieved a narrower band gap (2.16 eV) and significantly higher electrical conductivity (3600 S/m). This demonstrates that the choice of chelating agent is an effective way to fine-tune the material's properties. When tested as photoanodes in dye-sensitized solar cells with natural dyes, all films worked successfully. The best performance was achieved with the quercetin dye, yielding a power conversion efficiency of 0.26%. This result validates $CuSnO_3$ as a functional, eco-friendly, and cost-effective material for photoelectrode applications. Future work on optimizing film thickness and device interfaces promises to significantly boost this efficiency, paving the way for scalable renewable energy applications.

REFERENCES

1. Jiao X, Li S, Lv Z, Jiao H, He J, Song J. Advances of indium tin oxide in catalysis and cell. *Mater Today Commun*. 2025;44(January):112058. doi:10.1016/j.mtcomm.2025.112058
2. Kyriakides E, Nicolaou C, Ioannou PS, Papagiorgis P, Itskos G, Giapintzakis J. Single-stage fabrication of buffer and window layers of CIGS thin-film solar cells using pulsed laser deposition. *Sol Energy*. 2024;283(October):112993. doi:10.1016/j.solener.2024.112993
3. Cultrera A, Serazio D, Fabricius N, Callegaro L. New IEC standards for the measurement of sheet resistance on large-area graphene using the van der Pauw and the in-line four-point probe methods. *Meas J Int Meas Confed*. 2024;236(April):114980. doi:10.1016/j.measurement.2024.114980
4. Kim BN, Seo GK, Hwang SW, et al. Photophysical properties and photoelectrochemical performances of sol-gel derived copper stannate ($CuSnO_3$) amorphous semiconductor for solar water splitting application. *Ceram Int*. 2018;44(2):1843-1849. doi:10.1016/j.ceramint.2017.10.119
5. Salah M, Murphy P, Hall C, Francis C, Kerr R, Fabretto M. Pure silicon thin-film anodes for lithium-ion batteries: A review. *J Power Sources*. 2019;414(November 2018):48-67. doi:10.1016/j.jpowsour.2018.12.068
6. Kim BN, Seo GK, Hwang SW, et al. Corrigendum to 'Photophysical properties and photoelectrochemical performances of sol-gel derived copper stannate ($CuSnO_3$) amorphous semiconductor for solar water splitting application' [Ceramics International (2018) 1843–1849](S027288421732312X)(10.1016/. *Ceram Int*. 2018;44(5):5822. doi:10.1016/j.ceramint.2017.12.135
7. Liang Z, Wu W, Fang Z, et al. A review of doped metal oxide semiconductors in the stability of thin film transistors. *J Alloys Compd*. 2025;1010(November 2024):177434. doi:10.1016/j.jallcom.2024.177434
8. Zhang W, Yang X, Qu Z, et al. Influence of annealing atmosphere on optical and electrical properties of Ga-doped ZnO powders. *Phys B Condens Matter*. 2022;634(January):114926. doi:10.1016/j.physb.2022.413818
9. Rezania M, Moradnezhad H, Panahandeh M, Rahimpoor Kami MJ, Rahmani A, Hosseini BV. Effects of Diethanolamine (DEA) and Glass Fibre Reinforced polymer (GFRP) on setting time and mechanical properties of shotcrete. *J Build Eng*. 2020;31(November 2019). doi:10.1016/j.jobe.2020.101343
10. Zhu H, Li Y, Liu W, et al. Amorphous bimetallic oxide $CuSnO_3$ modified In_2O_3 for highly sensitive detection of thermal runaway marker 1,2-dimethoxyethane in lithium batteries. *Ceram Int*. 2025;51(8):9978-9986. doi:10.1016/j.ceramint.2024.12.430
11. Aminullah MW, Setiawan H, Huda A, Samaulah H, Haryati S, Bustan MD. Pengaruh Komposisi Material Semikonduktor Dalam Menurunkan Energi Band Gap Terhadap Konversi Gelombang Mikro. *J EECCIS*. 2019;13(2):65-70.
12. Hessam R, Najafisayar P. A comparative study on the microstructural feature and band-gap value of FeOOH and α-Fe_2O_3 films electrodeposited at different temperatures. *Heliyon*. 2026;12(1). doi:10.1016/j.heliyon.2025.e44414
13. Mondal R, Mondal S, Tudu P, et al. Tunable band gap, CB and VB positions of multicomponent Se65-xTe20Ge15Snx

chalcogenide glassy systems: Effect of metallic additives on physical and optical parameters. *Mater Chem Phys*. 2023;296(November 2022). doi:10.1016/j.matchemphys.2022.127187

14. Yasuda Y, Yamada Y, Koshiji F, Kobayashi S ichi, Uchida T, Hoshi Y. Effect of annealing treatment of indium tin oxide thin films on film properties and transparent antenna properties. *Thin Solid Films*. 2024;794(March):140295. doi:10.1016/j.tsf.2024.140295
15. Kiran Kumar SR, S H, P J, Jayanna BK, Yogesh Kumar K, Anantha MS. Evolution of SnO_2 nanoparticles for the electrochemical sensing of dopamine including photocatalytic toxic dyes degradation. *Sensors Int*. 2024;5(January):100278. doi:10.1016/j.sintl.2023.100278
16. Peng X, Xu R, Zhang L, Li X, Xu J, Huang D. Journal of Food Composition and Analysis Construction of multi-component CuO / ZIF-8 @ CNTs modified electrode for sensitive electrochemical detection of neohesperidin dihydrochalcone in liquor samples. 2026;151(February):0-10.
17. Rizaldi DR, Doyan A, Susilawati S. Sinteses lapisan tipis TiO_2:(F+In) pada substrat kaca dengan metode spin-coating sebagai bahan sel surya. *Orbita J Kajian, Inov dan Apl Pendidik Fis*. 2021;7(1):219. doi:10.31764/orbita.v7i1.4655
18. Sabriantie Mulus DA, Permana MD, Hayaa' Prawiranegara SP, et al. Enhanced performance of spin-coated silver-modified titanium dioxide thin films over dip coating method for metformin photodegradation. *Results Opt*. 2025;21(January). doi:10.1016/j.rio.2025.100838
19. Aouati R, Namoune D, Harouni S, et al. Al^{3+} doping effect on the properties of SnO_2 thin films prepared by sol-gel and dip-coating method for photocatalytic application. *Phys B Condens Matter*. 2026;723(September 2025):1-15. doi:10.1016/j.physb.2025.418089
20. Rahman M. Tin oxide thin films for the future: A paradigm shift in property engineering for advanced functional devices. *Next Mater*. 2025;9(October):101341. doi:10.1016/j.nxmate.2025.101341
21. Aliyaselvam O V., Mustafa AN, Azam MA, et al. Unveiling the prospect of copper iodide as hole transporting layer in perovskite solar cell by selective dopant strategy: A review. *Mater Sci Semicond Process*. 2025;197(May):109679. doi:10.1016/j.mssp.2025.109679
22. Kareem F, Chandrawati R, Ahmed MU. Tailoring nanocellulose: A comprehensive exploration of functionalisation with small, macro, and inorganic molecules for enhanced sensing and dual-mode biosensing. *Meas J Int Meas Confed*. 2025;239(January 2024):115499. doi:10.1016/j.measurement.2024.115499
23. Rusnadar AM, Qolbi AA, Widyabutama E, Jannah F, Shavira RA, Primadani DA. Pengujian Konduktivitas Listrik Material dangan Metode Four Point Probe (FPP). *Prakt Fis Lab Mater*. Published online 2015. https://www.studocu.id/id/document/institut-teknologi-sepuluh-nopember/fisika-dasar-i-physics/laporan-praktikum-laboratorium-fisika-mengenai-pengujian-konduktivitas-listrik-material-dengan-four-point-probe/45048221
24. Nofrizal N, Wulandari M, Impey S, Georgarakis K, Papanikolaou M, Raja PB. An experimental and simulation screening of X-65 steel weldment corrosion in high flow rate conditions. *Mater Today Commun*. 2024;39(March):108793. doi:10.1016/j.mtcomm.2024.108793
25. Wulandari M, Nofrizal N, Impey S, Georgarakis K, Raja PB, Hussin MH. The effect of corrosion inhibitor on X-65 steel weldment in high flow rate conditions. *Case Stud Chem Environ Eng*. 2024;10:100868. doi:10.1016/j.cscee.2024.100868
26. Agrawal A, Siddiqui SA, Soni A, Sharma GD. Advancements, frontiers and analysis of metal oxide semiconductor, dye, electrolyte and counter electrode of dye sensitized solar cell. *Sol Energy*. 2022;233(January):378-407. doi:10.1016/j.solener.2022.01.027